RESEARCH ARTICLE

Reconfigurable Intelligent Edges: Illuminating the Shadow Region in Wireless Networks

SIMON L. COTTON, (Senior Member, IEEE),
MUHAMMAD ALI BABAR ABBASI, (Member, IEEE),
GABRIEL G. MACHADO, (Member, IEEE), AND
OKAN YURDUSEVEN, (Senior Member, IEEE)

Centre for Wireless Innovation (CWI), Institute of Electronics, Communications and Information Technology (ECIT), Queen's University Belfast,
Belfast BT3 9DT, U.K.

Corresponding author: Muhammad Ali Babar Abbasi (m.abbasi@qub.ac.uk)

ABSTRACT This paper proposes a new wireless enabling technology for future smart radio environments. The approach aims to enhance signal coverage within the shadow region(s) of wireless networks with the aid of so-called 'reconfigurable intelligent edges (RIEs)'. RIEs may be installed at the fringes of shadowing objects such as buildings, walls and other obstacles which obscure the optical signal path from a transmitter to a receiver. We investigate two approaches to illuminating the shadow region in wireless networks using RIEs that exploit refraction or diffraction, operating in passive or active mode. The operation of RIE-assisted communications are investigated, in particular the ways they can redirect electromagnetic energy towards regions with little or no wireless network coverage. Following from this, a number of variations of RIEs are tested in real-world scenarios which consider illuminating the shadow region behind high-rise buildings, first in a city center, and then along a shoreline. Refractive RIEs in particular, are shown to provide significant gains compared to the case when no RIEs are involved, enhancing signal reception in the shadow region at street level behind a high-rise building by as much as 12 dB. Summary gain statistics are provided so that they can be easily included in system-level analyses and simulations. Critically, it is shown that reconfigurable intelligent edges offer a low complexity and cost-effective solution for improving connectivity in shadowing-limited environments.

INDEX TERMS 6G, B5G, diffraction, intelligent communication, microwave, millimetre-wave, refraction, shadowing, wireless communication.
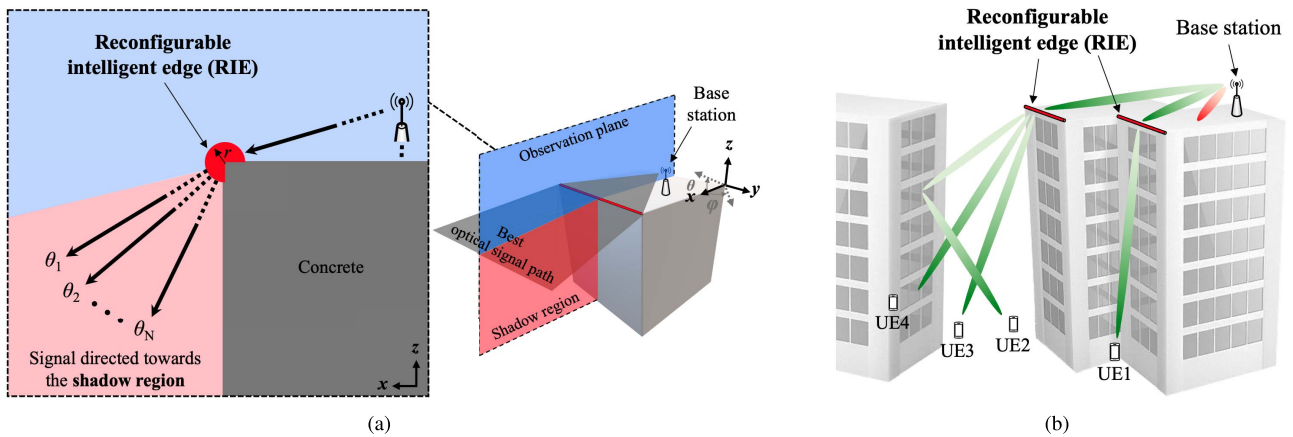
I. INTRODUCTION

In built-up environments, network operators often struggle to provide wireless users and devices with uninterrupted connectivity, and guaranteed quality of service. A primary reason for this is the lack of control of the physical characteristics and attributes which make up the wireless environment through which broadcast signals are propagated. Recognizing this challenge, and the potential performance enhancement opportunities, wireless designers are now weaving technologies which support the manipulation of propagated signals into the fabric of urban design. In the process, converting classical network coverage areas into intelligent communication and/or sensing environments [1].

Pathloss prediction models and algorithms have long considered the effects of electromagnetic (EM) wave propagation over buildings [2], [3], [4] and around corners in buildings [5], [6], [7]. Taking a dense city center environment as an example, buildings are often closely spaced and multiple stories high. Shadow regions are inevitable due to the high probability of the direct (optical) signal path between the base station (BS) and the wireless user being obscured (or blocked) by high-rise buildings or other obstacles residing in the environment. In these situations, any ensuing network coverage in the shadow region will most likely be the result of diffracted and/or scattered multipath which manages to

The associate editor coordinating the review of this manuscript and approving it for publication was Meng-Lin Ku.

101732

VOLUME 10, 2022

FIGURE 1. (a) Reconfigurable intelligent edge – concept and operation, (b) RIE-enabled wireless system serving multiple UEs in the shadow region.

circumvent the blocking structure. It is well-known that EM energy dissipation through propagation mechanisms such as diffraction and scattering tends to be greater than line of sight (or free-space) propagation and reflection [8], [9]. To limit the number of areas with poor or no network coverage in dense city center environments, understandably, over the last number of decades we have witnessed a progressive shrinking of cell sizes to micro-, pico- or even femtocell. However, this comes at significant cost as introducing new BSs requires specialized core network infrastructure and depending on the location may require extensive planning and approval.

Another method of dealing with this problem is to exploit the randomness in the radio environment by introducing advanced beamforming to existing BSs. Such a technique is now an integral part of 5G new radio and expected to play an increasingly important role in 6G wireless systems. Beamforming is shown to be especially useful when used in conjunction with reconfigurable intelligent surfaces (RISs); programmable structures that adapt the electric and magnetic properties of their surfaces to control signal propagation within wireless networks [10], [11], [12], [13]. RISs (also referred to as intelligent reflecting surfaces (IRSs)) can be realized through the dense packing of radiating elements, with separation distances smaller than half of the wavelength. This makes them work in a different way compared to other multi-element transmission technologies, e.g., phased arrays, multi-antenna transmitters, metasurfaces, and relays. A shadow region constantly being illuminated by an RIS will not require any additional phase shifting, significantly reducing transmission overheads [14]. Another attractive feature of RISs is the ease with which their placement and orientation can be optimized based on the targeted coverage requirements [15]. Nonetheless, depending on the method of implementation, they may need bulky periodic structures with thousands of unit cells and a DC biasing system deployed on planar surfaces, such as walls. Recently, there have been a number of works that have attempted to overcome the issue of diffraction loss in wireless systems. In [16] and [17], the authors have proposed the use of arrays of dipole antennas

fitted along the corner[1] of a building to exploit scattering and re-radiate impinging waves towards the shadow region. A multi-point approach, based on a series of repeaters (made up of two antennas and an amplifier), was presented in [18] to improve signal propagation through various stages of an indoor non-LOS wireless link at 2.45 GHz. Unlike [17], the repeaters were placed away from the corner so as to provide LOS links between the transmitter and repeater, and then the repeater and receiver.

Complementing these advances, in this work we propose an additional tool aimed at controlling signal propagation in future wireless networks. More specifically, we introduce the concept of a reconfigurable intelligent edge (RIE) that can be used to illuminate shadow regions in wireless networks. As we shall show in the sequel, RIEs can be fitted *directly* to building edges, are low-complexity and offer a cost-effective method of improving signal coverage in shadowing-limited environments with little or no network coverage. We introduce two types of RIE which operate by exploiting the physics of refraction and diffraction. Among the different ways that a refractive RIE can be developed include using active or passive frequency selective, band-gap or wideband materials [19], [20], [21], [22], while a diffractive RIE can be implemented using passive or reconfigurable corrugated, periodic or semi-periodic surfaces, developed using metallic or high conductivity materials [8], [9], [23], [24], [25]. Working within wireless networks, such as 6G, RIEs can be made to work intelligently, for example, by judiciously controlling their excitation, or if supported, adaptively tuning their electrical properties or structure in orchestration with network demands.

II. RIE-ENABLED SMART RADIO ENVIRONMENTS

Fig. 1(a) demonstrates the operation of an RIE in the context of a cellular system. Here a BS antenna purposely illuminates the RIE which is fixed at the boundary of the face and roof of a

---

[1]In [17], the dipole structures were placed at a separation of 0.8 to 1 wavelength from the corner of the building.

high rise building so as to redirect the transmitted EM energy from the BS towards the shadow region behind the building. In this instance, we consider the RIE to have a $\frac{3}{4}$ cylindrical structure,[2] with a radius of r. The RIE, shown in red in Fig. 1(a), is attached to the edge of a concrete building. It is assumed to be capable of redirecting the EM energy arriving from the BS along chosen 'bending' angles $\theta_1, \theta_2, \ldots, \theta_N$ illuminating the shadow region, while the redirectivity is assumed to remain consistent along the y-axis for every angle θ. Using this approach simplifies the 3-dimensional (3D) redirectivity problem to a 2D one and allows a thorough investigation of the functionality of the RIE, discussed further in section III.

The system level operation of the RIE involves the combined effort of beamforming at the BS and redirectivity at the RIE, to extend the network coverage in to the shadow region. An example RIE-enabled smart radio environment is illustrated in Fig. 1(b) in which a roof-top BS is responsible for illuminating multiple RIEs in response to demand from a number of user equipment (UE) operating in the shadow region of the buildings with respect to the BS.

III. RECONFIGURABLE INTELLIGENT EDGE CLASSIFICATION

In this section RIEs are classified according to the physical mechanism that they use to redirect EM energy received from a BS. In this paper, we consider r to range between 0.5λ to 1.5λ for the RIE structures. Here λ denotes the wavelength at the operating frequency. This selection is made to ensure that the investigated RIE structures have practical dimensions to be attached to the edge of a building while offering sufficient electrical size to manipulate the BS radiated electromagnetic wave-fronts as will be shown in the following sub-sections.

A. PASSIVE REFRACTIVE RIE

This is the simplest class of the RIE which relies primarily on the properties of the material it is constructed from and the (reconfigurable) angle of excitation from the BS. In a passive refractive RIE, the impinging EM energy is basically absorbed by the material and then redirected in the desired direction, hence two boundary conditions apply. The maximum directivity direction can be defined by controlling the refractive index of the material n (where $n = \sqrt{\epsilon_r(\omega)}$, ϵ_r is the relative permittivity of the material and ω is the angular frequency). Thus, tailored dispersion characteristics of the material used to develop the refractive RIE can be exploited.

To explore the impact of n on the RIE's refraction characteristics, consider a test signal impinging upon the refractive RIE, with a relative permeability of 1. For the sake of simplicity, using the coordinate system definition in Fig. 1(a), we consider the case where the impinging signal arrives parallel to the x-axis, while the results are observed in the xz-plane. The time harmonic incident, scattered and refracted
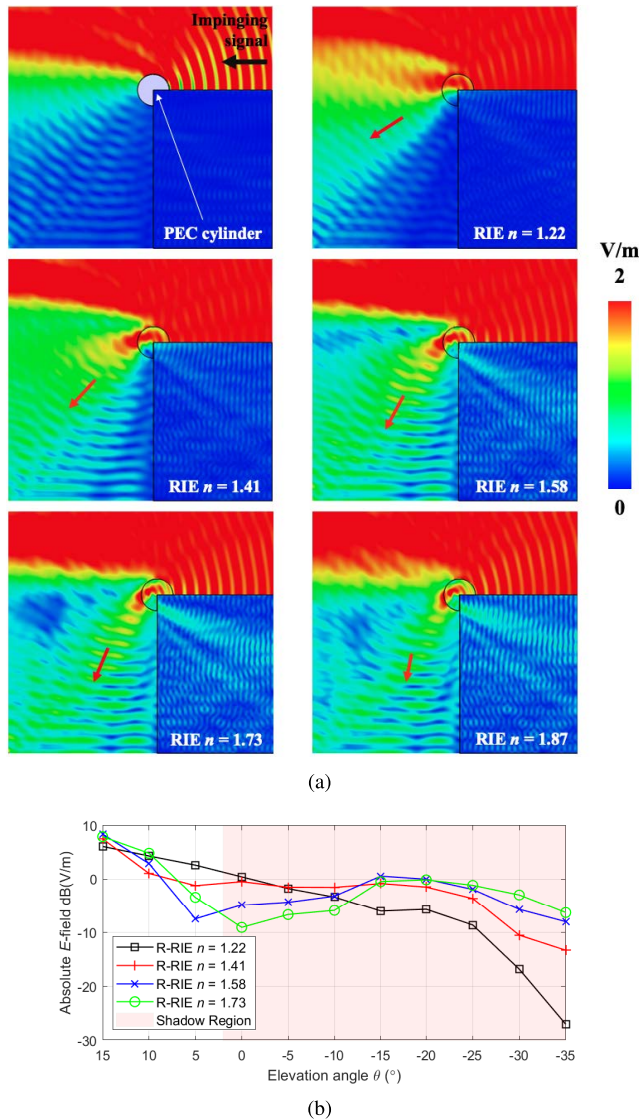
E-field is surface plotted to measure the extent of the shadow region being illuminated by an RIE of radius $r = 2/3\lambda$.

Fig. 2(a) presents results in terms of the maximum E-field, simulated using the finite element method (FEM) (see [26] and references therein for mathematical formulations). Before considering the RIE, a perfect electric conductor (PEC) cylinder of $r = 2/3\lambda$ is used to create a benchmark for comparison. As expected, fields of the range ~ 1 V/m are diffracted along the x-axis, while very little EM energy is diffracted towards the shadow region. When the PEC is replaced by a passive refractive RIE, using a material with known n, a higher average magnitude to E-field can be seen to be directed towards the shadow region. As n increases, the angle of peak directivity from the $+x$-axis increases, however, there is a limit to the extent that the shadow region can be illuminated. For example, taking $n > 1.7$, it is observed that a portion of the redirected EM energy begins to get absorbed within the concrete. Considering $\theta = 0°$ aligned to x-axis, across the intermediate bending angles, ranging from $0°$ to $-20°$ (Fig. 2(b)), the passive refractive RIE with $n = 1.41$ can be seen to provide relatively uniform coverage. For the more extreme bending angles (e.g. $\theta < -20°$) RIEs with higher values of n can be used to provide coverage, however they do this in a more focused manner, i.e. with a reduced angular spread of the signal. Remarkably, the results verify that a passive refractive RIE with a radius as small as $\frac{2\lambda}{3}$ is capable of providing enhanced radio coverage within the shadow region. In addition to the examples shown in Fig. 2, and given the refractive nature of the RIE material, it will be shown in later sections that wave-fronts with different (i.e. reconfigurable) angles of incidence on the RIE yield similar coverage within the shadow regions. This suggests that an RIE operating in conjunction with beamforming capable BSs will be a promising solution for expanding radio coverage, even when the RIE is passive.

B. PASSIVE DIFFRACTING RIE

This second class of RIE acts to enhance the *diffraction* at the building edge. Classical diffraction models such as knife edge or equivalent geometric structure diffraction have shown that small amounts of EM energy are diffracted towards wireless users situated behind single or multiple obstacles [8], [9]. For the first time, we show how to enhance this diffraction with an aid of an RIE. Consider the case where the RIE cylinder shown in Fig. 1 is replaced by a cylindrical numerical PEC of $r = 1\lambda$ [4], [27], [28], and illuminated by a plane wave impinging at an angle of $45°$ from the $-x$-axis. The goal of an RIE is to keep a portion of the impinging EM energy *locked* on the surface, and release it towards the shadow region. Theoretically, this can be achieved by converting the smooth PEC surface into a 'bumpy' one, however two additional factors need to be considered. First, the actual area illuminated by any impinging wave is curved, so the standard boundary conditions for a periodic bumpy surface [23] can not be applied directly. This is especially the case when r is comparable to the λ. Secondly, given the curved cylindrical
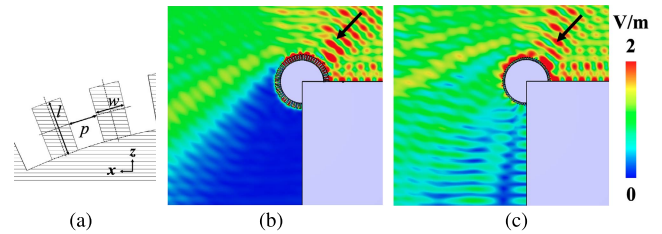
---

[2]It is worth highlighting that the RIE is not limited to a cylindrical structure and other geometrical configurations are also possible.

(a)

(b)

FIGURE 2. (a) Simulated *E*-field when a plane wave parallel to *x*-axis impinges on a (concrete) building corner equipped with a passive refractive RIE. (b) *E*-field strength vs elevation angle across the shadow region.

FIGURE 3. (a) Passive diffractive RIE surface structure, (b) and (c) simulated *E*-field when a plane wave impinges on a building corner equipped with a passive diffractive RIE.

same corrugated surface featuring a *l* of $\sim 0.1\lambda$, approximating a so-called *rough conducting interface* [25] can be seen to enhance the diffraction, as shown in Fig. 3(c). As argued in [29], the majority of the power factor of the surface wave propagating through the corrugated metal sheet is determined by the shape of the uppermost part of the roughness. Hence, a curved corrugated RIE surface, with longer *l* and a wider gap between the plates, results in low effective capacitance along the outer edge, making it a high impedance surface. When *l* is reduced, it increases the effective capacitance, helping to lock the propagating wave. Thus, in Fig. 3(c), the outer edge of the RIE can be seen to have the highest value of *E*-field, where surface waves become locked, and are then slowly released towards the shadow region. This phenomenon governs the operation of a passive diffractive RIE.

C. ACTIVE REFRACTIVE RIE
Changing the effective *n* of a material is an active area of research [19]. Future innovations here will create smart materials and surfaces, paving the way for active refractive RIEs which can be retuned in response to requests to illuminate different portions of the shadow region. Under this regime, two different types of aperture can be considered, the first, in which the receiving aperture area is planar, and second, in which receiving aperture area is curved. One approach to creating an active refractive RIE with a planar surface area is to use layers of metasurfaces with periodic or quasi-periodic sub-wavelength structures, capable of redirecting the incident wave towards the desired direction.

A number of approaches to create layered structures and their associated active controls are given in [20], [30], and [31]. One such approach is to implement layers with switching capabilities. Each layer is then programmed to slightly tilt the impinging signal, channelling it in the desired direction of propagation. It is worth highlighting that while conceptually relatively straightforward, the practical implementation of such an RIE will be non-trivial as a number of boundary conditions between sandwiched layers apply, requiring extensive hardware considerations. Also, due to the number of layers, higher insertion losses are to be expected. To develop an active RIE with a curved surface facing the impinging signal, one option is to divide the RIE cylinder

surface of the RIE, a very limited amount of EM energy can remain as surface waves and contribute to the desired enhanced diffraction because the overall receiving *aperture area* is small.

In the example simulations in Fig. 3, a narrow surface-wave bandgap sheet such as corrugated surface [23], [24] is imprinted on a PEC RIE. Here, the gap between two parallel plates is *p*, the plate length is *l* and the plate width is *w* (Fig. 3(a)). The surface in Fig. 3(b) in planar configuration has the ability to *lock* an impinging plane wave at an angle of 45° from the −*x*-axis, locking it to the surface and creating a surface wave. The same surface, using a curved configuration, appears to be incapable of creating additional diffracted signal components to be propagated towards the desired shadow region (Fig. 3(b)). However, the
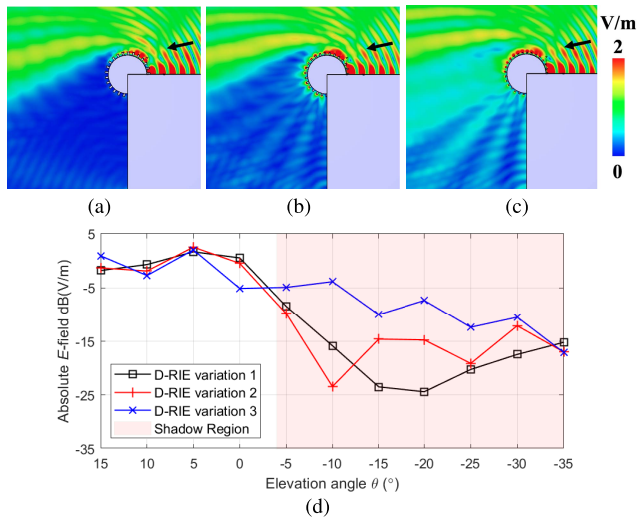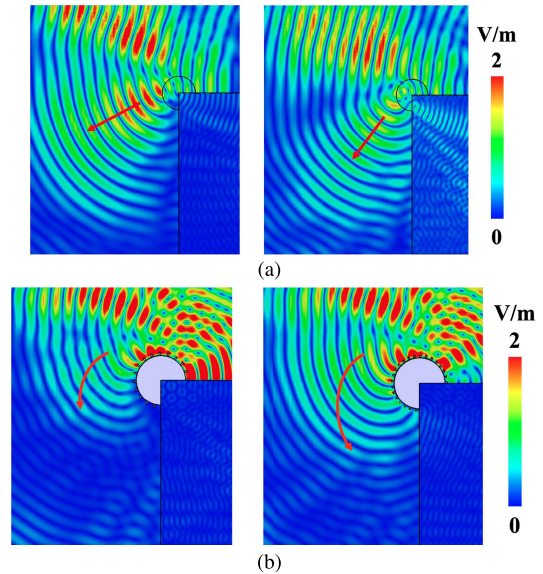
FIGURE 4. Simulated *E*-field for a diffractive RIE with $r = \lambda$ and (a) $p = 0.16\lambda$, $w = 0.05\lambda$, $l = 0.10\lambda$, (b) $p = 0.16\lambda$, $w = 0.06\lambda$, $l = 0.13\lambda$, and (c) $p = 0.16\lambda$, $w = 0.04\lambda$, $l = 0.10\lambda$. (d) *E*-field strength vs elevation angle across the shadow region.

FIGURE 5. Instantaneous *E*-field map (normalized to 2 V/m) showing (a) high directivity coverage in the shadow region using a refractive RIE, and (b) low directivity wider area coverage in the shadow region using a diffractive RIE.

into multiple sectors or quadrants with tunable refraction properties to achieve the desired effective n. Such advances in dielectric interface techniques are discussed in [21], [32], and [33]. These approaches can be exploited to realize refractive responses similar to the ones shown in Fig. 2. Another option is to compensate for the imaginary part of the active refractive RIE's surface impedance as a function of the inter-element separation distance of an array of spherical dielectric particles having sub-wavelength radii [22]. If tunability is achieved, such RIE can handle multiple incident impinging angles, making it a universal solution for smart radio environments.

D. ACTIVE DIFFRACTIVE RIE

As discussed in section III-B, controlling the capacitance of the top layer of a corrugated surface creates the ability to translate impinging waves into surface waves. The gap between two plates in the corrugated surface can be regarded as a parallel-plate transmission line, running across the surface of the RIE, and shorted at the bottom. In theory, a quarter wavelength slot between two parallel plates can be converted into an open-circuit one [24]. Similarly, a range of equivalent capacitances on the top layer of a curved corrugated surface can be achieved by varying the length l from 0 to $\lambda/4$. Note that capacitance in a corrugated surface can also be achieved by changing p or even w, while keeping l constant, giving rise to a number of reconfigurability options using tunable electronics implemented on the diffractive RIE surface. One representative RIE is shown in Fig. 4, where three corrugated surface conditions are shown to sequentially enhance the diffraction capability of the RIE. One important point to note is that the periodicity of the corrugated surface is constant in this example, which results in the locked EM energy leaving the corrugated surface sequentially as can
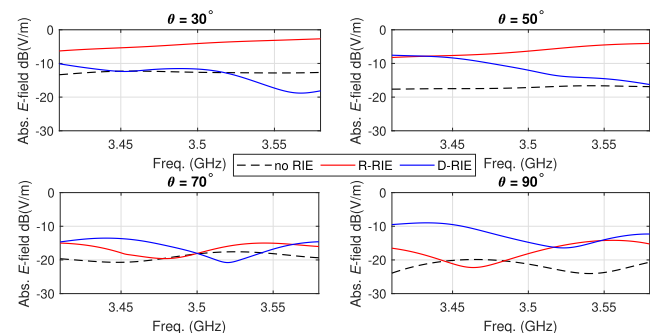
FIGURE 6. Simulated *E*-field versus frequency along multiple bending angles when a building corner is equipped with an R-RIE and a D-RIE.

be seen in Figs. 4 (a) - (c). One way around this is to break the periodicity and create a high impedance along the RIE surface where the incident wave is impinges and decreases the impedance along the corrugated RIE surface. Another way is to create a curved, sinusoidally modulated, impedance surface on the RIE (similar to the planar version in [34]). Nevertheless, the goal of improved signal strength within the shadow region is achievable as shown in Fig. 4(d).

IV. SOME OPERATIONAL CONSIDERATIONS

Based on our initial analysis, to provide directive coverage within a shadow region, active or passive refractive type RIEs show the most promise (see Fig. 5(a)). This will be advantageous in scenarios where the network knows the approximate location of wireless users and can adapt the 'bending' angle accordingly. Correspondingly, to achieve wider coverage across the entire shadow region (and hence

low directivity), passive or active diffractive RIEs are a better option (Fig. 5(b)). Clearly, this form of transmission will be most beneficial in situations where the location of wireless users is unknown or cannot be estimated in advance.

Some additional operational considerations are important to note. First, the overall aperture area on the RIEs considered here is likely to be much smaller compared to widely proposed reflecting (e.g. RIS) or refracting surfaces (e.g., transmissive metasurfaces). Hence, the impinging signal's power may need to be higher, meaning that for many practical implementations, a focused beam of energy will be required for the excitation of RIE. Secondly, the RIE is expected to maintain its performance within a bandwidth, say for instance, in sub-bands of 5G n73, say 3.46 - 3.48 GHz and 3.50 - 3.54 GHz (see Fig. 6). However, for wider bandwidths, e.g., considering the entire 3.41 - 3.58 GHz band, the operation is expected to vary over extended frequencies. Lastly, the proposed active RIE configurations will require specialised hardware capable of tuning the relevant parameters, but the flexibility they provide in expanding the radio coverage is expected to be greater than that of the passive RIEs.

V. SOME REAL-WORLD EXAMPLES

In the previous sections, RIEs were classified and analyzed using FEM which enabled a clear visualization of the electric field in close proximity of the building for different RIE configurations. For a full scale simulation of a real-world scenario, the use of finite elements, finite difference time domain or method of moments (MoM) would be computationally expensive. Therefore, in this section, we have utilized ray-tracing as an alternative, to investigate the additional gain provided by the RIEs compared to the case where no RIE is used to illuminate the shadow region above the ground (street) level and along the sides of buildings. The first real-world example scenario (Scenario I) considered a city center environment. Here, we used data freely available from OpenStreetMaps [35] to replicate a full-scale section of Belfast City in the United Kingdom, as shown in Fig. 7(a). In our system, the RIE is irradiated by a BS situated on the roof of a high-rise building, as depicted in Fig. 1(b). Subsequently, the propagating signal is rebroadcast from the RIE (or building edge in the case that no RIE is used), acting as the ray launcher in our simulations. In Scenario I the selected building edge was located on top of the Grand Central Hotel building, which is 80 m tall and separated from another building located on the opposite side of the street by 22 m (Fig. 7(c)).[3]

The second real-world example scenario (Scenario II) was created to replicate a beach-front (or equivalently shoreline) environment where high-rise buildings dominate the

---

[3]For illustrative purposes, also shown in Fig. 7(c) is a 2D section of the equivalent pattern of the Refractive RIE ($n = 1.41$), later referred to as Refractive RIE A, superimposed on the building structure.
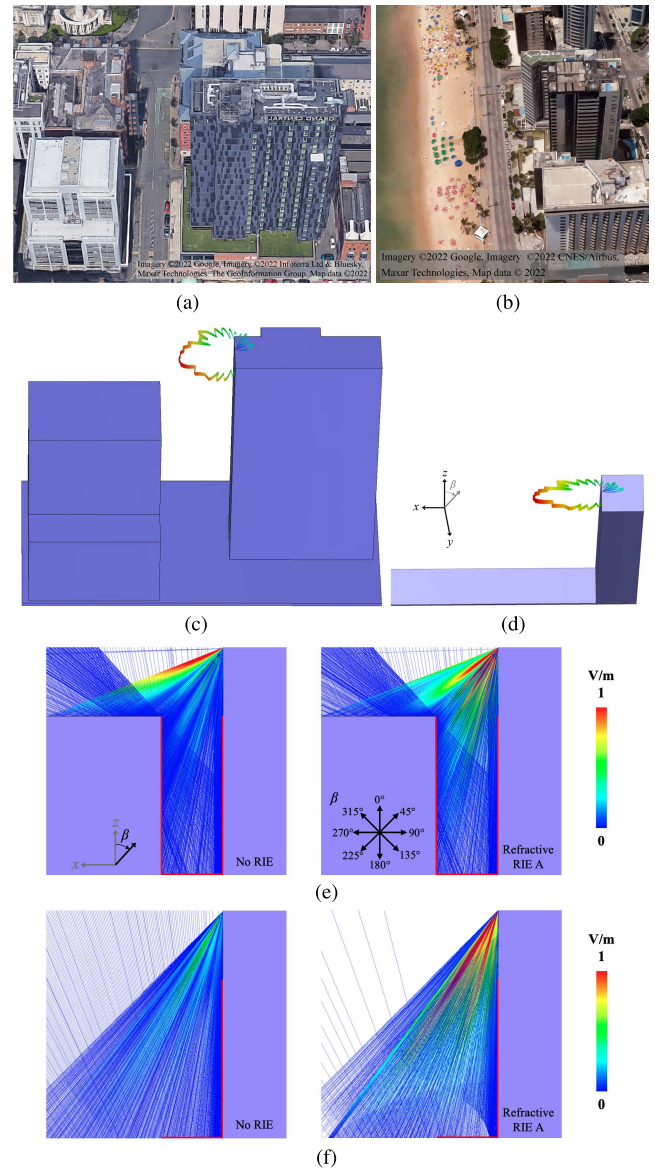
FIGURE 7. Simulated real-world examples: (a) 3D images extracted from Google Maps for Scenario I and; (b) Scenario II; (c) CST model used for ray tracing in Scenario I and; (d) Scenario II, with overlaying resultant far-field patterns on the building corners (note: 2D plot is not normalized); (e) Example ray tracer output with Refractive RIE A in Scenario I and; (f) Scenario II, where the red lines along the edges of the building and above street level (1 m & 1.5 m) indicate the lines followed by the probe locations.

shoreline (e.g. as found in Miami Beach in the USA and Recife in Brazil, Fig. 7(b)). For this case, and to keep consistency with the analysis conducted for the city center environment, an 80 m tall building was placed at the edge of a 22 m street, as depicted in Fig. 7(d). In contrast to the previous example (Scenario I), there were no buildings on the opposing side of the street. The choice for the distance between the building and the roadside pathway was based on a survey of satellite images from different cities, which were consistently between 22 and 24 m, except for places where hotels with pools are located at the beach.

A. SIMULATION SET-UP

We used the Asymptotic Solver (A-Solver) available within CST Studio Suite to simulate the two example scenarios. In the A-Solver, lossy materials, such as concrete, are not natively supported; therefore we used a lossless dielectric material of permittivity $\epsilon_r = 4.47$, corresponding to CST's first order fit for the dielectric constant of concrete, whilst also placing perfect matching layers (PML) boundary conditions around the structure to absorb the rays which penetrated the material. Moreover, to increase the accuracy of the modelled scenario and reduce computation time, the PML boundaries were limited to a width of 1 m, and extended 1 m from within the concrete layers, which included the ground. Farfield sources obtained from a small-scale FEM simulation (such as previously depicted in Figs. 2 – 5) were used in conjunction with the ray launcher. The farfield sources for the refractive and diffractive RIEs were placed at a distance of $\frac{\lambda}{3}$ and $\frac{\lambda}{2}$ from the building corner, respectively. These farfield source locations are the centre of the effective aperture areas of the refractive and diffractive RIEs, respectively. The simulation frequency chosen for Scenarios I and II was 3.5 GHz as specified in 5G New Radio [36].

In Figs. 7(c) and (d), which depict Scenarios I and II, respectively, the ground-floor edge of the building (with the RIE) is located at the origin of the coordinate system and the receiving probes are placed along the xz-plane. For Scenario I, the probes on the street were placed to form a 'U-shape', starting from the top of the right building, following the front face of the structure down to street level, then across the street, and ending on the top of the left building. The street level probes start from the right building (adjacent to the building wall) and are uniformly spaced 2 cm from each other until the left building (see red contour in Fig. 7(e)). Two sets of probes were placed on the street, one at an elevation of $z = 1$ m and the other at $z = 1.5$ m. The street level locations were chosen to be representative of the signal received by a UE located in the pocket (1 m) or being handheld (1.5 m) of a pedestrian crossing the street. The vertical probes were located corresponding to the floors of the building. Here it is assumed the floor height is 3 m, meaning that the vertical distances $z = 0, 3, 6, \ldots,$ m represent the ground floor, first floor, second floor etc. The probes were then placed at 1 and 1.5 m elevation from each floor (again representing a UE in the pocket and being handheld, respectively). For Scenario II, the probes running along the side of the left building (Scenario I), were removed, as no building was located on the opposite side of the street to the building with the RIE. Note that the probes used in this study are polarization agnostic, meaning that they can receive signals in any polarization.

In the A-Solver, 10175688 Shooting and Bouncing Rays (SBR) were used in both Scenarios I and II, with a maximum of 3 reflections permitted. A total of 5 simulations were performed for each scenario, where we compared the E-field strength received at the probes for the 'No RIE'

(a)   (b)

FIGURE 8. Illustration of the street level zones used for the analysis in (a) Scenario I in front of the Grand Central Hotel building in Belfast City, UK and (b) Scenario II in front of Edf. Vânia building in Recife, Brazil.

case, Refractive RIEs with $n = 1.44$ and $n = 1.73$ (see Fig. 2), and the Diffractive RIEs variations 2 and 3 (see Fig. 4) with a normalized amplitude of 1 V/m used for the farfield sources in all simulations. An example of the output of the ray tracer for Scenarios I and II is given in Fig. 7(e) and (f), respectively. For ease in referencing, henceforth, the refractive RIEs with $n = 1.44$ and 1.73 will be termed refractive RIE A and B, respectively. Similarly, the diffractive RIE variations 2 and 3 will be termed as diffractive RIE A and B, respectively.

B. SIMULATION RESULTS AND DISCUSSION

The results obtained from the ray tracing performed in CST were post-processed in Matlab, by converting the simulated E-Field measured by the probes using

$$P_X = 10\log_{10}\left(\frac{|E|^2}{\eta_0}\right) \text{ (dB)}, \qquad (1)$$

where P_X is the power density measured in Watts/m^2 at each probe, $X \in \{$No RIE, Refractive RIE A, Refractive RIE B, Diffractive RIE A, Diffractive RIE B$\}$, and $\eta_0 = 120\pi$ is the free-space impedance measured in Ohms.

As discussed previously, one of the key challenges in cellular networks is ensuring sufficient coverage at street level in dense city center environments. This is often hampered by the close proximity of tall buildings, as depicted in Fig. 7, which can shadow signal transmissions from the BS positioned on the top of the high-rise structures. To investigate the ability of RIEs to support BS transmissions in this case, we now employ four of the RIE variations introduced in Section III. In our analysis, we split the street level into three distinct zones as shown in Fig. 8.[4] These are: Zone 1, which considers the section of the street closest to the building with the RIE; Zone 2, which is made up of the central area of the street in between the two buildings; and Zone 3, which is the section of the street closest to the building on the opposite side of the street. For our analysis Zones 1, 2 and 3 covered the distances (intervals) [0 m, 7.333 m), [7.333 m, 14.6667 m) and [14.6667 m, 22 m), where 0 m is the closest

[4]Image courtesy: Google Earth, Data SIO, NOAA, U. S. Navy, NGA, GEBCO Maxar Technologies landset/Copernicus TerraMetrics and CNES/Airbus.
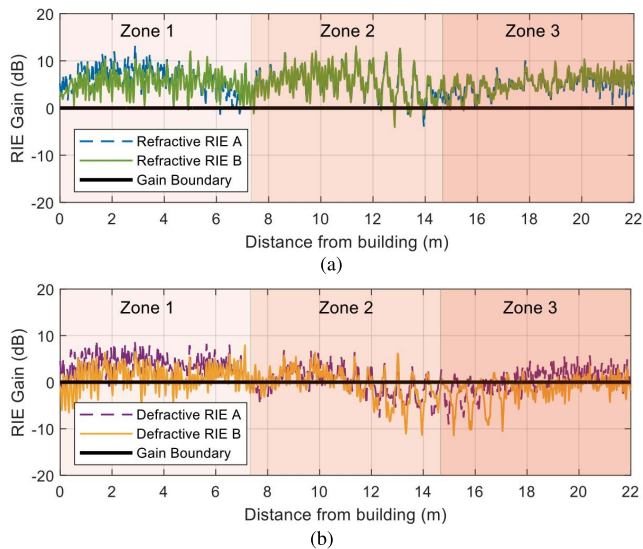
FIGURE 9. RIE gain (dB) vs distance from building (meters) at 1 m elevation from street level in the city center environment (Scenario I) considering: (a) refractive RIEs A and B, and (b) diffractive RIEs A and B.

point to the building with the RIE. All zones are obviously within the shadow region of the building fitted with the RIE (and BS).

To conduct our analysis, we make use of the RIE gain calculated at each distance (d), which is defined as

$$\text{IE Gain}_{\text{dB}}(d) = P_X(d) - P_{\text{No IE}}(d), \qquad (2)$$

where P_X and $P_{\text{No IE}}$ are defined in (1).

We first consider Scenario I. Fig. 9 shows the RIE gain experienced 1 m above street level compared with the distance from the base of the building fitted with the RIE. As we can see from the plots (Fig. 9(a)), both refractive RIEs offer improved gain in Zone 1 compared to the no RIE case (i.e. their traces are in the positive region above the 'gain boundary'), achieving an RIE gain greater than 10 dB. From Fig. 9(b), we can also see that in close proximity (between 0 and 1 m) to the building fitted with the RIE, diffractive RIE A provided improved gain compared to diffractive RIE B which struggled to outperform the no RIE case, suggesting that it may offer little benefit for illuminating the shadow region closest to a building. However beyond this (between 1 and 7.333 m), both diffractive RIEs generally performed better than the no RIE case, although not to the same extent as the refractive RIEs. In the central region between the two buildings, i.e. Zone 2, we can see that the performance of refractive RIEs A and B was largely identical, with both consistently offering over 6 dB enhanced gain over the majority of the region compared to the no RIE case (Fig. 9(a)), which is approximately equivalent to quadrupling the received power. In this zone, both diffractive RIEs struggled to deliver a significant improvement in the gain, except for a small distance between 9 and 11 m. This pattern of signal enhancement was repeated in Zone 3, where again both refractive RIEs continually performed better than the no RIE case,

whereas diffractive RIE A only provided a marginal improvement and diffractive RIE B consistently performed worst overall.

These observations are confirmed by the empirical cumulative distribution functions (CDFs) given in Fig. 10. As can be seen from Fig. 10(a), in Zone 1, both refractive RIEs deliver a signal enhancement over nearly 100% of the shadow region covered by Zone 1 compared to the no RIE case. As shown in Table 1,[5] the mean RIE gains for refractive RIEs A and B in Zone 1 are 6.07 dB and 5.26 dB, respectively. Interestingly, both of the diffractive RIEs are shown to provide an enhancement over 70% of the shadow region covered by Zone 1, although as discussed above, the RIE gains are much lower than those delivered by the refractive RIEs, suggesting that for this type of scenario, refractive RIEs are the best option for illuminating the shadow region closest to the base of the building. Fig. 10(b) provides the empirical CDFs of the RIE gain in the central region between the two buildings (Zone 2). Here we can see that the refractive RIEs again offer the best performance, with both guaranteeing a signal enhancement for 95% of the shadow region covered by Zone 2 compared to the no RIE case. In Zone 2, the performance of both diffractive RIEs was degraded compared to Zone 1, with both being outperformed by the no RIE case for approximately 50% of the zone. In Zone 3, both refractive RIEs performed similar to Zone 1, offering increased RIE gain across the entire zone, with mean RIE gains of 4.90 dB (refractive RIE A) and 5.20 dB (refractive RIE B). Diffractive RIE A outperformed the no RIE case for at least 65% of the shadow region covered by Zone 3, however, as before the benefits here were marginal (mean RIE gain = 1.25 dB, Table 1). In this region, the diffractive RIE B performed poorer than the no RIE case offering a degradation in the mean RIE gain = −1.55 dB (Table 1). For completeness, Fig. 10(d) shows the empirical CDFs of the RIE gains calculated over the entire region between the two buildings (i.e. *Zone 1 + Zone 2 + Zone 3*). With the exception of diffractive RIE B, the majority of the empirical CDF plots reside in the positive half of the figure, providing strong evidence for the use of reconfigurable intelligent edges to enhance signal coverage in shadowed regions at street level within city center environments.

Fig. 11 provides a sample of the empirical CDF plots for the case when the probes are situated: (a) 1.5 m above street level[6]; (b) at the front face of the 'left' building on the opposite side of the street to the building with the RIE fitted and; (c) at the front face of the 'right' building, i.e. the building with the RIE fitted. Again, in all three cases, the refractive RIEs provide favorable performance, outmatching the no RIE case in the majority of cases. Following a similar trend to results discussed so far, diffractive RIE A performed best achieving signal enhancements for around 70%

---

[5]Tables 1 to 6 provide summary statistics for the RIE gain, which can conveniently be incorporated as an additional gain parameter in system-level analyses and simulations.

[6]For brevity, we only show the aggregated results for this case, however, a summary of the RIE gain statistics are provided in Table 2.
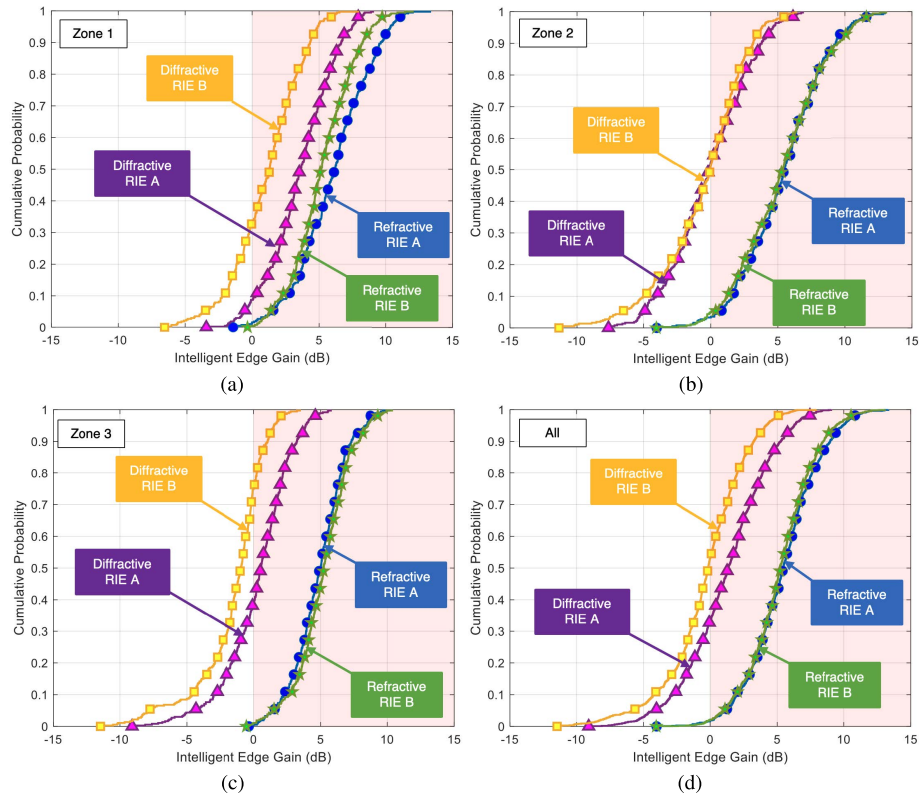
FIGURE 10. Empirical CDFs showing the distribution of the RIE gain for the different reconfigurable intelligent edge structures within (a) zone 1 (same side of street to building), (b) zone 2 (central region), (c) zone 3 (opposite side of street to building) and (d) across all zones, with the UE operating at 1 m elevation from street level in the city center environment (Scenario I).
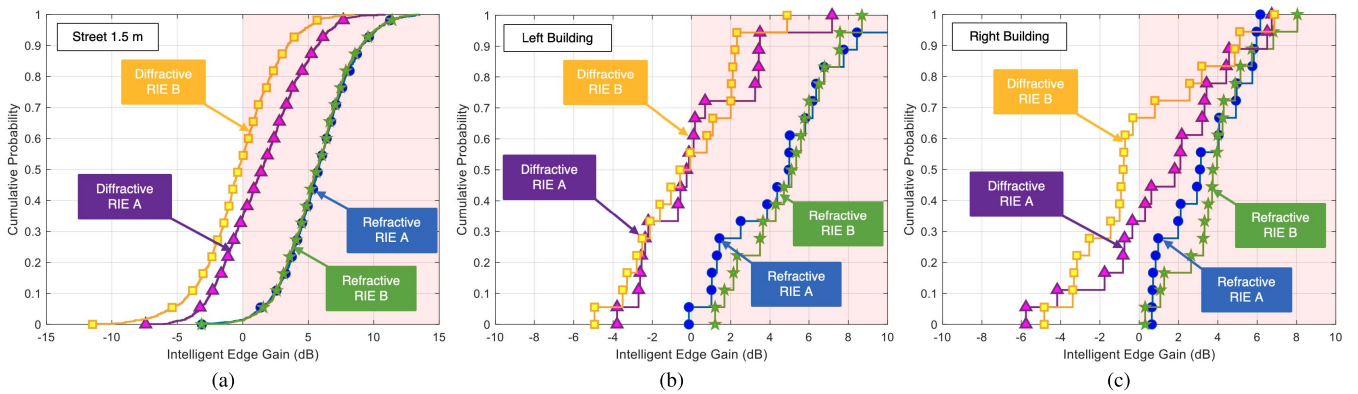
FIGURE 11. Empirical CDFs showing the distribution of the RIE gain for the different reconfigurable intelligent edge structures in the city center environment (Scenario I) considering (a) 1.5 m elevation from street level and, (b) the front face of the left building and, (c) the front face of the right building.

of the shadow region for cases (a) and (c), however it struggled to improve coverage into the building on the opposite side of the street to the RIE. As shown in Tables 2 and 3, diffractive RIE B proved ineffective in the majority of the cases considered here, on average degrading the overall performance.

Previously, in Scenario I, the building on the opposite side of the street acted to contribute additional signal components

to the field strength. In environments such as beach fronts (Fig. 7(b)) or at the peripheries of city centers, the propagation geometry may mean that signal components arriving at the receiver are primarily the result of propagation around the building edge or those reflected from the ground. To investigate this Scenario II, we replicated the simulation performed above, except in this instance, no building was positioned on the opposite side of the street (Fig. 7(d)). Again the street

TABLE 1. Mean (Av.) and Standard Deviation (std.) of the RIE Gain in decibels at 1 m elevation from street level in the city center environment (Scenario I). Note maximum and minimum mean RIE gains are highlighted in green and pink respectively.

Zone	Refractive RIE A (*n* = 1.41) Av. (dB)	std. (dB)	Refractive RIE B (*n* =1.73) Av. (dB)	std. (dB)	Diffractive RIE A Av. (dB)	std. (dB)	Diffractive RIE B Av. (dB)	std. (dB)
1	6.07	2.70	5.26	2.28	3.57	2.39	1.08	2.57
2	5.40	3.00	5.29	3.13	-0.10	2.97	-0.57	3.21
3	4.90	1.97	5.20	2.01	0.27	2.51	-1.55	2.55
All	5.46	2.63	5.25	2.52	1.25	3.10	-0.35	3.00

TABLE 2. Mean (Av.) and Standard Deviation (Std.) of the RIE Gain in decibels at 1.5 m elevation from street level in the city center environment (Scenario I). Note maximum and minimum mean RIE gains are highlighted in green and pink respectively.

Zone	Refractive RIE A (*n* = 1.41) Av. (dB)	Std. (dB)	Refractive RIE B (*n* =1.73) Av. (dB)	Std. (dB)	Diffractive RIE A Av. (dB)	Std. (dB)	Diffractive RIE B Av. (dB)	Std. (dB)
1	6.68	2.61	6.44	2.32	4.33	2.05	1.52	2.65
2	5.40	2.93	5.32	3.08	-0.01	2.66	-0.74	3.00
3	5.16	2.09	5.25	2.12	0.18	2.30	-1.72	2.33
All	5.75	2.65	5.67	2.60	1.50	3.09	-0.31	3.00

TABLE 3. Mean (Av.) and Standard Deviation (Std.) of the RIE Gain in decibels at the front of the left and right buildings in the city center environment (Scenario I). Note maximum and minimum mean RIE gains are highlighted in green and pink respectively.

Zone	Refractive RIE A (*n* = 1.41) Av. (dB)	Std. (dB)	Refractive RIE B (*n* =1.73) Av. (dB)	Std. (dB)	Diffractive RIE A Av. (dB)	Std. (dB)	Diffractive RIE B Av. (dB)	Std. (dB)
Left Building	4.58	2.95	4.91	2.16	0.22	2.91	-0.28	2.63
Right Building	3.26	2.03	3.88	1.91	1.42	3.37	0.01	3.28

TABLE 4. Mean (Av.) and Standard Deviation (Std.) of the RIE Gain in decibels at 1 m elevation from street level in the beach front environment (Scenario II). Note maximum and minimum mean RIE gains are highlighted in green and pink respectively.

Zone	Refractive RIE A (*n* = 1.41) Av. (dB)	Std. (dB)	Refractive RIE B (*n* =1.73) Av. (dB)	Std. (dB)	Diffractive RIE A Av. (dB)	Std. (dB)	Diffractive RIE B Av. (dB)	Std. (dB)
1	5.25	2.12	5.04	2.00	1.88	3.03	0.22	2.70
2	3.18	2.36	6.09	1.12	0.07	2.45	-0.20	1.50
3	8.63	2.42	8.96	2.10	4.34	2.51	0.12	1.65
All	5.69	3.22	6.70	2.44	2.10	3.20	0.05	2.03

TABLE 5. Mean (Av.) and Standard Deviation (Std.) of the RIE Gain in decibels at 1.5 m elevation from street level in the beach front environment (Scenario II). Note maximum and minimum mean RIE gains are highlighted in green and pink respectively.

Zone	Refractive RIE A (*n* = 1.41) Av. (dB)	Std. (dB)	Refractive RIE B (*n* =1.73) Av. (dB)	Std. (dB)	Diffractive RIE A Av. (dB)	Std. (dB)	Diffractive RIE B Av. (dB)	Std. (dB)
1	5.77	1.70	7.48	2.08	3.04	2.87	1.07	2.79
2	3.45	1.89	6.17	0.93	0.20	2.39	-1.46	1.64
3	8.71	2.64	9.10	2.35	4.06	2.61	-0.49	1.88
All	5.98	3.02	7.58	2.24	2.43	3.09	-0.29	2.39

TABLE 6. Mean (Av.) and Standard Deviation (Std.) of the RIE Gain in decibels at the front face of the right building in the beach front environment (Scenario II). Note maximum and minimum mean RIE gains are highlighted in green and pink respectively.

Zone	Refractive RIE A (*n* = 1.41) Av. (dB)	Std. (dB)	Refractive RIE B (*n* =1.73) Av. (dB)	Std. (dB)	Diffractive RIE A Av. (dB)	Std. (dB)	Diffractive RIE B Av. (dB)	Std. (dB)
Right Building	2.44	2.81	3.44	2.83	1.21	4.55	-0.28	3.72

level was segmented into three zones (i.e. Zones 1, 2 and 3) using the same distances (intervals) used in Scenario I. Fig. 12 shows the RIE gain experienced 1 m above street level compared with the distance from the base of the building fitted with the RIE for the beach environment. From the figure, it is clear that both refractive RIEs outperform the no
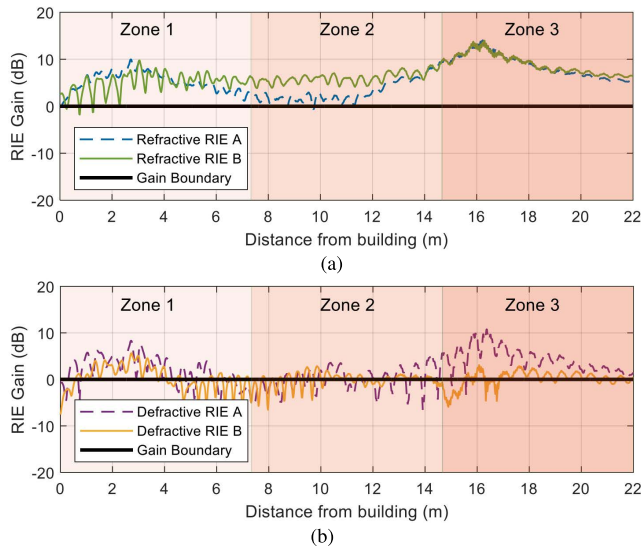
FIGURE 12. RIE gain (dB) vs distance from building (meters) at 1 m elevation from street level in the beach front environment (Scenario II) considering: (a) refractive RIEs A and B, and (b) diffractive RIEs A and B.

RIE case across all three zones (Fig. 12(a)). What is most striking, is the significant RIE gain that can be achieved, notably in Zone 3 where both refractive RIEs A and B provide between 5 and 12 dB of RIE gain. Of the two diffractive RIEs, diffractive RIE A performs best in the beach environment, particularly in Zone 3, farthest from the building with the RIE, achieving RIE gains of up to 10 dB (Fig. 12(b)). Despite this, it is observed that both diffractive RIEs struggle in the central region, i.e. Zone 2, with no improvement over the no RIE case.

Another important observation from Fig. 12 (beach front environment) is the more gradual variations in the RIE gain compared with Fig. 9 (city center environment). This is the result of the reduced number of multipath components (MPCs) in the beach front environment, caused by the lack of a tall structure on the opposite side of the street to the building with the RIE fitted to it. The origin of this can be seen clearly in Fig. 7(e) and (f), which show example ray traces for refractive RIE A, where the high number of interacting MPCs in the city center environment leads to more rapid variations in the RIE gain.

Fig. 13 provides the empirical CDFs of the RIE gain in the beach front environment. As we can see from Figs. 13(a) to (d), both refractive RIEs provide a positive RIE gain over more than 99% of the coverage area. This confirms the observations made above and reinforces the benefit of using a refractive RIE to help provide signal coverage in the shadow region behind buildings. This is further supported by the mean RIE gain figures provided in Table 4, which were between 5.25 dB and 8.96 dB, assuming the optimum refractive RIE is chosen. Thus having some method of actively adapting the refractive index of the RIE will be of extreme benefit. Contrasting the performance of the refractive RIEs in the beach front environment to the city

center environment, we can see that in nearly all cases (where the optimal refractive RIE was chosen), the RIE gain for the beach front was greater than that achieved in the city center. From Fig. 13, we can see that both diffractive RIEs offered poorer performance than the refractive RIEs, with refractive RIE B performing worst overall. Lastly, and for completeness, Fig. 14 provides the empirical CDFs of the aggregated RIE gain for (a) 1.5 m above street level and; (b) the face of the 'right' building, i.e. the building with the RIE fitted, with the corresponding summary statistics provided in Tables 5 and 6. Here we can see that the refractive RIEs again outperform the diffractive RIEs, however it is worth pointing out that diffractive RIE A still managed to provide a positive RIE gain for over 70% of the shadow regions at the street level and the front face of the building.

VI. EXAMPLE CHANNEL SNAPSHOTS

As we have seen in Section V.B, RIEs have significant potential to enhance signal reception in regions behind large shadowing objects such as high-rise buildings. As part of the propagation manipulation process, they will also impact the channel as observed by the receiver, in this case, in the downlink. To illustrate how RIEs can alter the channel, we present some snapshots of the characteristics of the downlink signal as experienced in the city center environment for a selection of receiver positions above ground level and along the sides of the buildings. For the study, we focused on time and angle dispersion characteristics which are important in wideband systems (e.g. to understand the potential impact of effects such as intersymbol interference (ISI)) as well as beamforming systems (to understand the most likely angle of arrival (AOA) and the degree of signal spreading across the angular domain). For brevity, we only consider refractive RIE A in our analysis since it was observed to show the most promising results based on the analysis performed in Section V.B. To conduct the channel simulations, we used the same setup as described in Section V.A, however in this instance instead of electric field probes as receivers (or equivalently UEs), we used isotropic receivers to enable antenna coupling calculations and channel parameters to be computed within the CST A-solver. To obtain the channel snapshots we used 7 isotropic receivers for the 1 m above ground level (and again for 1.5 m above ground level) simulations. In this instance, the receivers were placed at the center and boundaries of each zones defined in Section V.A. The receivers along the sides of the buildings were positioned 3 m apart, from ground level upwards.

Figs. 15(a) and (b) show an example of the power delay profiles (PDPs) obtained at the receivers (or equivalently UEs) positioned 3.66 metres apart, 1 m above ground level across the entire street (i.e. boundary and center of zones 1, 2 and 3 combined) for the case where no RIE is used and, when refractive RIE A is used, respectively. As is common practice in channel studies, to calculate the PDP, we determined the excess delay of each arriving signal component
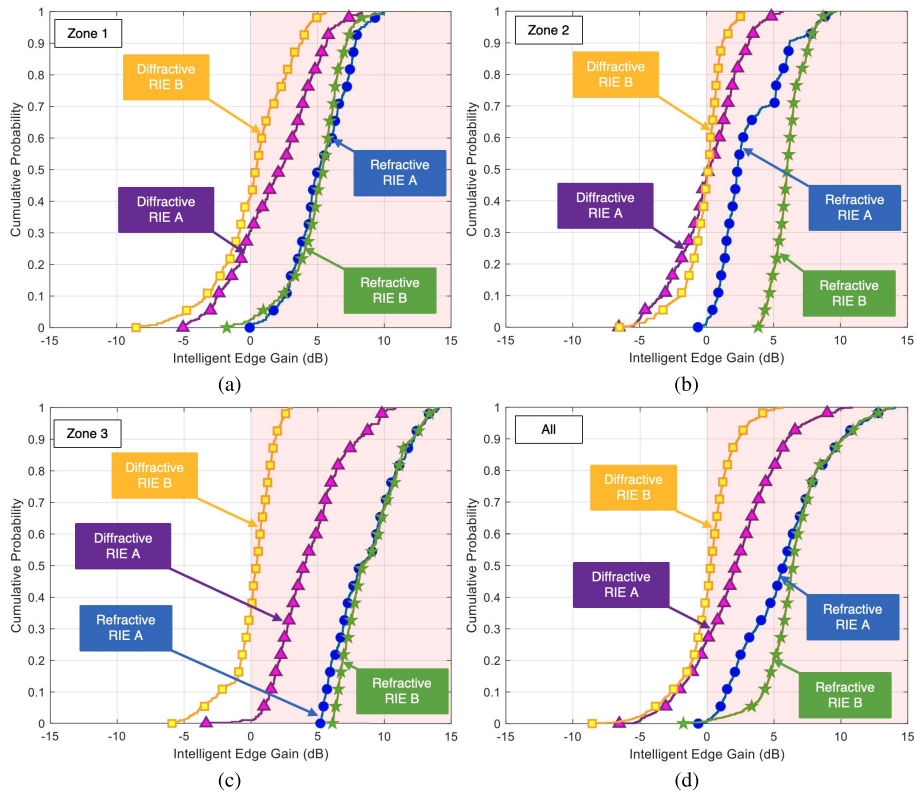
FIGURE 13. Empirical CDFs showing the distribution of the RIE gain for the different reconfigurable intelligent edge structures at 1 m elevation from street level in the beach environment (Scenario II): (a) zone 1 (same side of street to building), (b) zone 2 (central region of street), (c) zone 3 (opposite side of street to building) and (d) across all zones.
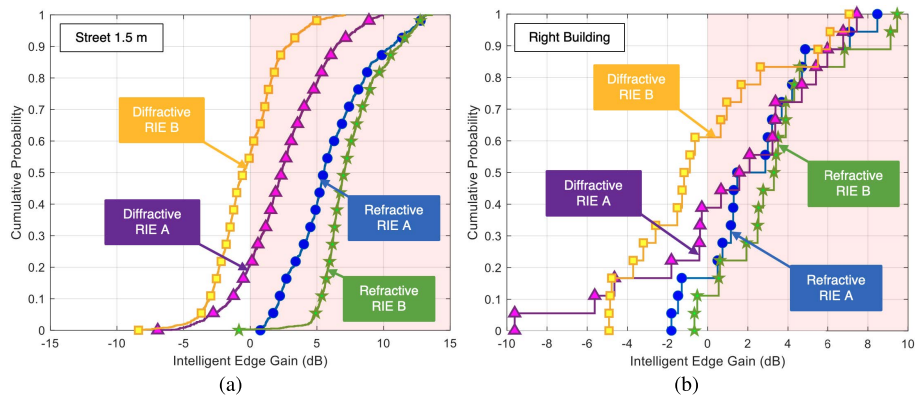

FIGURE 14. Empirical CDFs showing the distribution of the RIE gain for the different reconfigurable intelligent edge structures in the beach environment (Scenario II) considering (a) 1.5 m elevation from street level and, (b) 1 m from the front face of the right building.

relative to the first arriving signal component. One immediate observation from Fig. 15 is the significantly higher powers of the signal components arriving at the UEs when the RIE is used compared to the no RIE case. This is apparent for all of the early arriving components across positions 1 to 7, supporting the observations made above in relation to the RIEs improving the received signal in deeply shadowed regions behind high-rise buildings.

Another observation from Fig. 15 is the different numbers of MPCs which are detected at the UE. For practical purposes, we set the noise threshold at a level of -120 dBm, meaning that any signal components that arrived with a power less than this value were disregarded as it is unlikely they would make a meaningful contribution to the received signal. We can see in Fig. 15(b) that many more signal components arrive at the UE compared to Fig. 15(a). In some cases, MPCs,
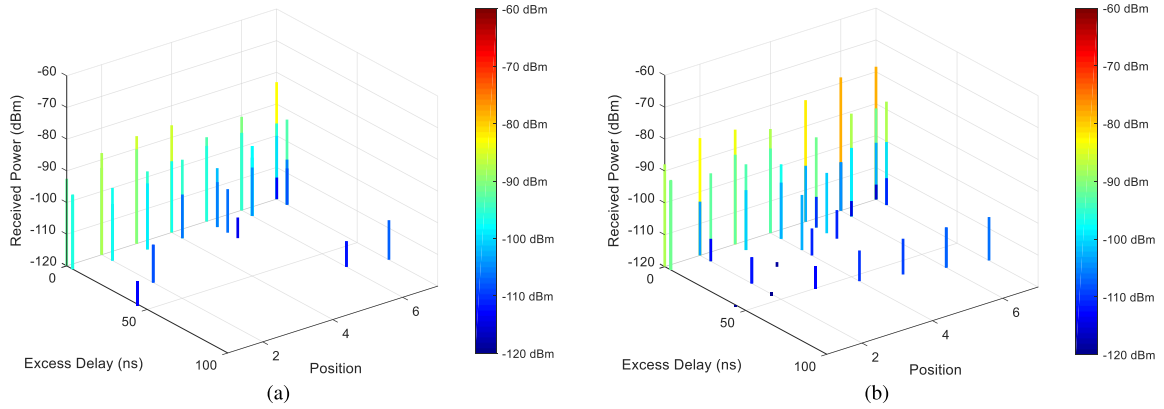
FIGURE 15. (a) PDPs showing the excess delay of the signal components arriving at the UE (for positions 1 to 7) from the top edge of the building closest to the base station (i.e. the no RIE case), (b) identical scenario except in this case refractive RIE A is placed at the top edge of the building. Note, to assist with the interpretation of the plots, the signal components are color coded according to the power that they contribute to the received signal.
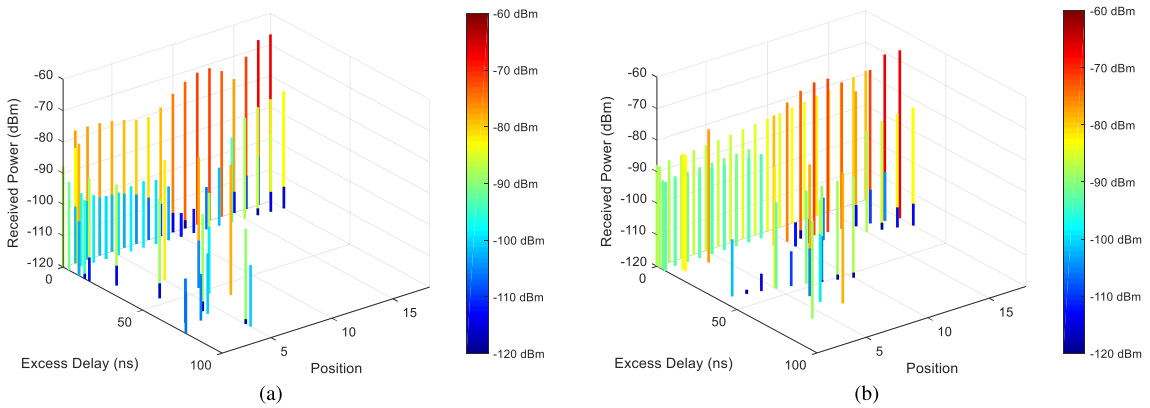
FIGURE 16. (a) PDPs showing the excess delay of the signal components arriving at the receiver positions on the front face of the left building and, (b) the front face of the left building when refractive RIE A is placed at the top edge of the building closest to the base station. Note, to assist with the interpretation of the plots, the signal components are color coded according to the power that they contribute to the received signal.

TABLE 7. Summary delay dispersion statistics.

Scenario		Av. mean excess delay time (ns)	Std. of the mean excess delay time (ns)	Av. RMS delay spread (ns)	Std. of the RMS delay spread (ns)	Av. maximum excess delay (ns)	Std. of the maximum excess delay (ns)
1 m above ground	No RIE	1.26	0.59	3.56	1.34	34.75	25.98
	Refractive RIE A	1.07	0.46	3.18	0.90	55.31	10.18
1.5 m above ground	No RIE	2.19	1.97	5.10	3.26	43.70	23.68
	Refractive RIE A	1.63	0.56	3.71	1.08	54.75	11.48
Left Building	No RIE	5.25	8.33	18.71	22.00	176.12	91.45
	Refractive RIE A	7.71	10.69	20.05	9.89	180.10	91.54
Right Building	No RIE	15.23	6.50	13.79	10.40	165.94	128.21
	Refractive RIE A	17.58	13.29	14.17	8.07	193.01	117.75

which were present for the no RIE case, are no longer present in the case when refractive RIE A was used. The greater number of MPCs in Fig. 15(b) shows that the use of an RIE in scenarios where UEs are operated close to ground level opens up opportunities for additional signal paths to be created (see discussion of the RMS angle spread below), which

may be beneficial for beamforming systems attempting to re-establish broken links by seeking alternative signal paths in the angular domain [37].

In wireless systems design, two key metrics for determining the likely impact of ISI are the mean excess delay, denoted $\bar{\tau}$, and the RMS delay spread, denoted σ_τ. The mean
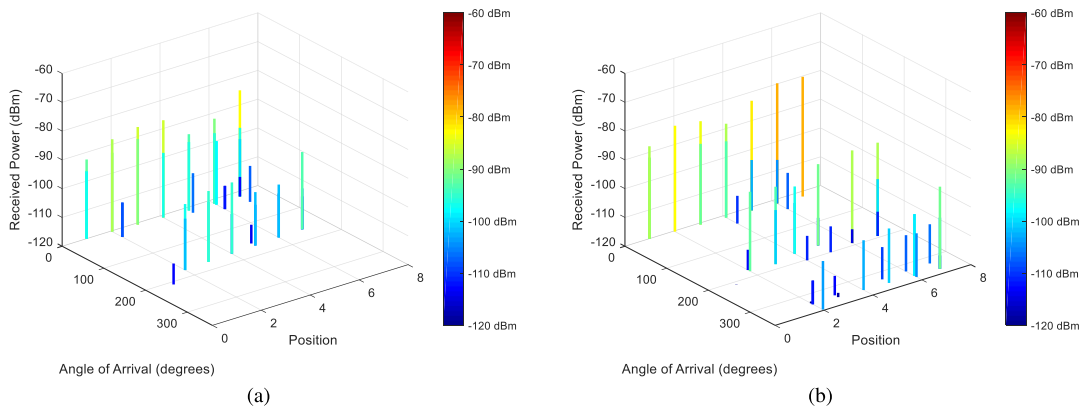
FIGURE 17. (a) PAPs showing the AOA of the signal components arriving at the UE (for positions 1 to 7) from the top edge of the building closest to the base station (i.e. the no RIE case), (b) identical scenario except in this case refractive RIE A is placed at the top edge of the building. Note, to assist with the interpretation of the plots, the signal components are color coded according to the power that they contribute to the received signal.

TABLE 8. Summary angular dispersion statistics.

Scenario		Av. mean angle (°)	Std. of the mean angle (°)	Av. RMS angle spread (°)	Std. of the RMS angle spread (°)
1 m above ground	No RIE	22.03	9.94	43.10	14.66
	Refractive RIE A	28.66	15.20	57.98	25.76
1.5 m above ground	No RIE	26.11	8.40	52.91	14.87
	Refractive RIE A	44.04	31.19	80.16	34.88
Left Building	No RIE	29.25	9.62	21.55	21.63
	Refractive RIE A	34.39	8.24	47.35	19.62
Right Building	No RIE	2.29	5.21	6.02	6.16
	Refractive RIE A	18.46	31.51	40.71	56.37

excess delay may be determined from the PDP as [38]

$$\bar{\tau} = \frac{\sum_{i=0}^{N-1} |\alpha_i|^2 \, \tau_i}{\sum_{i=0}^{N-1} |\alpha_i|^2}, \tag{3}$$

where $|\alpha_i|$ represents the amplitude and τ_i represents the excess delay of the ith multipath component, respectively. To calculate the RMS delay spread, we evaluate [38]

$$\sigma_\tau = \sqrt{\bar{\tau^2} - (\bar{\tau})^2}, \tag{4}$$

where,

$$\bar{\tau^2} = \frac{\sum_{i=0}^{N-1} |\alpha_i|^2 \, \tau_i^2}{\sum_{i=0}^{N-1} |\alpha_i|^2}. \tag{5}$$

Table 7 presents the average (av.) and the standard deviation (std.) of $\bar{\tau}$ and σ_τ computed across each of the scenarios considered above. As we can see, the average mean excess delay for the UE operating at 1 m and 1.5 m elevation from street level in the city center environment is very low, insinuating that the bulk of the power received arrives close to the first arriving component. The equivalent figures for the receivers positioned along the front face of the left and right buildings are larger, especially for the right building, suggesting that the significant contributing signal components are more spread out in the delay domain. This is supported by the average RMS delay spread which was much greater

for the signal illuminating the building faces compared to the UEs operating close to ground level. Fig. 16 illustrates this further, showing the PDPs recorded at the receiver positions spanning the left and right building faces. Here additional MPCs, enhanced by the RIE, and reflected off the sides of the building contribute significantly to the received power and increase the RMS delay spread. It is also worth highlighting that when used in the city center environment, the RIE causes an increase in the maximum excess delay time compared to the no RIE case. This is presumably due to the enhanced gain offered by the RIE, meaning that signal components that extend below the noise threshold, which would ordinarily not be sensed by the receiver, are now detected. This may or may not be problematic depending on data transmission rates and ISI countermeasures employed such as adaptive equalization [39].

Similar to the mean excess delay and RMS delay spread, equivalent metrics can be computed to understand signal dispersion in the angle domain. To characterize the angular spread of the MPCs in the city center environment, we computed the mean angle of arrival (AOA), $\bar{\beta}$, according to [38]

$$\bar{\beta} = \frac{\sum_{i=0}^{N-1} |\alpha_i|^2 \, \beta_i}{\sum_{i=0}^{N-1} |\alpha_i|^2}. \tag{6}$$

Following from equation 6, the RMS angle spread can be determined as

$$\sigma_\beta = \sqrt{\bar{\beta}^2 - (\bar{\beta})^2}, \qquad (7)$$

where,

$$\bar{\beta}^2 = \frac{\sum_{i=0}^{N-1} |\alpha_i|^2 \beta_i^2}{\sum_{i=0}^{N-1} |\alpha_i|^2}. \qquad (8)$$

As can be seen from Table 8, refractive RIE A acts to increase the mean angle compared to the no RIE case across all of the considered scenarios (see Fig. 7(e) for the angular reference system for AOA used in this study). Critically, the RIE also increases the RMS angle spread of the signal components arriving at the receivers in all scenarios. When combined with the significant RIE gains reported in Section V.B, this demonstrates the superior coverage that can be achieved by using an RIE to illuminate the shadow region behind high-rise buildings compared to no RIE. For completeness, Fig. 17 shows an example of the power angle profiles (PAPs) obtained for the UE positioned 1 m above ground level across the entire street. The much richer set of AOAs promoted by refractive RIE A (Fig. 17(b)) compared to the no RIE case (Fig. 17(a)) is clearly evident, reinforcing the point made above about exploiting the angular diversity created by RIEs along with directional wireless systems to overcome shadowing.

VII. CONCLUSION AND FUTURE WORK

Providing radio coverage behind large obstacles and structures continues to be one of the key challenges for network designers wishing to provide ubiquitous access to wireless services. To help address and overcome this, for the first time, we have introduced the concept of a reconfigurable intelligent edge, which can be placed on the fringes of buildings to alter the natural propagation of radio signals. Specifically, we have introduced two classes of RIE, namely refractive and diffractive, which exploit the physics of refraction and diffraction, respectively, to help redirect radio signals and provide illumination in the shadow region. To accelerate future design and adoption, we have also highlighted some techniques and emergent technologies that could be used to operate RIEs in a passive or active manner. Based on our initial investigation, it was found that passive or active refractive RIEs, can be used to provide directive coverage within the shadow region. This will be beneficial in cellular networks when the approximate location of users relative to the building edge is known in advance of signal transmission. Where this information is not known or cannot be estimated in advance, passive or active diffractive RIEs will be able to provide wider signal coverage across the shadow region, albeit at the cost of reduced gain.

To understand the improvement in wireless network coverage that could be achieved in a real-life setting using RIEs, we have conducted full-scale ray tracing simulations of city center and beach front environments using the well-established asymptotic method. From our analysis it is shown

that choosing the right RIE configuration (e.g. refractive index or corrugated surface structure) can lead to considerable signal enhancements in both environments. Overall, it was found that the RIE gain (that is the improvement compared to the case where no RIE is present) was greatest for refractive RIEs. These performed best in practice, offering a mean gain of at least 5.20 dB, with instantaneous gains of up to 12 dB across the shadow region for a user at street level (1 m) in both environments. It is worth remarking that although we have demonstrated the RIE concept for rooftops in a cellular setting, the same principles apply for manipulating signal propagation around building corners (e.g. to assist device-to-device communications [40]) and by extension within indoor environments to assist with wireless local area network (WLAN) coverage [41].

As with any new technology, many unanswered questions remain. For instance, the successful adoption of RIEs will require a greater knowledge of the relationship between their geometrical and material properties and signal re-directivity. Determining how these structures perform at different frequencies, and how they can be made sufficiently broadband (e.g. to provide seamless coverage across cellular bands) will be paramount. Understanding how RIEs can be integrated into future smart radio environments will also be important, in particular, how they can be used to augment other propagation manipulating technologies such as RISs. This will require determining their role in increasing capacity, improving reliability and reducing latency. The next stage of this work will include the physical implementation and testing of RIEs using layered surfaces. This will incorporate further detailed channel studies to understand how the inclusion of RIEs impacts the end-to-end spectral efficiency in both outdoor cellular and indoor WLAN settings.

REFERENCES

[1] M. Di Renzo, M. Debbah, D.-T. Phan-Huy, A. Zappone, M.-S. Alouini, C. Yuen, V. Sciancalepore, G. C. Alexandropoulos, J. Hoydis, H. Gacanin, and J. D. Rosny, "Smart radio environments empowered by reconfigurable ai meta-surfaces: An idea whose time has come," *EURASIP J. Wireless Commun. Netw.*, vol. 2019, no. 1, pp. 1–20, 2019.

[2] H. Xia, H. Bertoni, L. Maciel, R. Rowe, A. Lindsay-Stewart, and L. Grindstaff, "Urban and suburban microcellular propagation," in *Proc. 1st Int. Conf. Universal Pers. Commun.*, 1992, pp. 1–2.

[3] J. Walfisch and H. L. Bertoni, "A theoretical model of UHF propagation in urban environments," *IEEE Trans. Antennas Propag.*, vol. AP-36, no. 12, pp. 1788–1796, Dec. 1988.

[4] V. Daniele, G. Lombardi, and R. S. Zich, "The double PEC wedge problem: Diffraction and total far field," *Trans. Antennas Propag.*, vol. 66, no. 12, pp. 6482–6499, Dec. 2018.

[5] D. Chizhik, G. J. Foschini, M. J. Gans, and R. A. Valenzuela, "Keyholes, correlations, and capacities of multielement transmit and receive antennas," *IEEE Trans. Wireless Commun.*, vol. 1, no. 2, pp. 361–368, Apr. 2002.

[6] K. Kalliola, H. Laitinen, P. Vainikainen, M. Toeltsch, J. Laurila, and E. Bonek, "3-D double-directional radio channel characterization for urban macrocellular applications," *IEEE Trans. Antennas Propag.*, vol. 51, no. 11, pp. 3122–3133, Nov. 2003.

[7] J. Du, D. Chizhik, R. A. Valenzuela, R. Feick, G. Castro, M. Rodriguez, T. Chen, M. Kohli, and G. Zussman, "Directional measurements in urban street canyons from macro rooftop sites at 28 GHz for 90% outdoor coverage," *IEEE Trans. Antennas Propag.*, vol. 69, no. 6, pp. 3459–3469, Jun. 2021.

[8] S. Deng, G. R. MacCartney, and T. S. Rappaport, "Indoor and outdoor 5G diffraction measurements and models at 10, 20, and 26 GHz," in *Proc. IEEE Global Commun. Conf. (GLOBECOM)*, Dec. 2016, pp. 1–7.

[9] T. Negishi, V. Picco, D. Spitzer, D. Erricolo, G. Carluccio, F. Puggelli, and M. Albani, "Measurements to validate the UTD triple diffraction coefficient," *IEEE Trans. Antennas Propag.*, vol. 62, no. 7, pp. 3723–3730, Jul. 2014.

[10] M. Di Renzo, A. Zappone, M. Debbah, M.-S. Alouini, C. Yuen, J. De Rosny, and S. Tretyakov, "Smart radio environments empowered by reconfigurable intelligent surfaces: How it works, state of research, and the road ahead," *IEEE J. Sel. Areas Commun.*, vol. 38, no. 11, pp. 2450–2525, Nov. 2020.

[11] E. Björnson, Ö. Özdogan, and E. G. Larsson, "Reconfigurable intelligent surfaces: Three myths and two critical questions," *IEEE Commun. Mag.*, vol. 58, no. 12, pp. 90–96, Dec. 2020.

[12] L. Dai, B. Wang, M. Wang, X. Yang, J. Tan, S. Bi, S. Xu, F. Yang, Z. Chen, M. Di Renzo, and C. B. Chae, "Reconfigurable intelligent surface-based wireless communications: Antenna design, prototyping, and experimental results," *IEEE Access*, vol. 8, pp. 45913–45923, 2020.

[13] Q. Wu, S. Zhang, B. Zheng, C. You, and R. Zhang, "Intelligent reflecting surface-aided wireless communications: A tutorial," *IEEE Trans. Commun.*, vol. 69, no. 5, pp. 3313–3351, May 2021.

[14] V. Jamali, G. C. Alexandropoulos, R. Schober, and H. V. Poor, "Low-to-zero-overhead IRS reconfiguration: Decoupling illumination and channel estimation," *IEEE Commun. Lett.*, vol. 26, no. 4, pp. 932–936, Apr. 2022.

[15] S. Zeng, H. Zhang, B. Di, Z. Han, and L. Song, "Reconfigurable intelligent surface (RIS) assisted wireless coverage extension: RIS orientation and location optimization," *IEEE Commun. Lett.*, vol. 25, no. 1, pp. 269–273, Jan. 2021.

[16] R. Zabihi, C. G. Hynes, and R. G. Vaughan, "Simple dipole scatter for filling a shadow region," in *Proc. IEEE Int. Symp. Antennas Propag. North Amer. Radio Sci. Meeting*, Jul. 2020, pp. 1091–1092.

[17] R. Zabihi, C. G. Hynes, and R. G. Vaughan, "Enhanced coverage in the shadow region using dipole scatterers at the corner," *IEEE Trans. Antennas Propag.*, vol. 69, no. 11, pp. 7771–7781, Nov. 2021.

[18] J. Oh, M. Thiel, and K. Sarabandi, "Wave-propagation management in indoor environments using micro-radio-repeater systems," *IEEE Antennas Propag. Mag.*, vol. 56, no. 2, pp. 76–88, Apr. 2014.

[19] A. Nemati, "Tunable and reconfigurable metasurfaces and metadevices," *Opto-Electron. Adv.*, vol. 1, no. 5, 2018, Art. no. 180009.

[20] F. Ding, Y. Yang, R. A. Deshpande, and S. I. Bozhevolnyi, "A review of gap-surface plasmon metasurfaces: Fundamentals and applications," *Nanophotonics*, vol. 7, no. 6, pp. 1129–1156, 2018.

[21] S. Sun, W. Yang, C. Zhang, J. Jing, Y. Gao, X. Yu, Q. Song, and S. Xiao, "Real-time tunable colors from microfluidic reconfigurable all-dielectric metasurfaces," *ACS Nano*, vol. 12, pp. 2151–2159, Feb. 2018.

[22] A. Monti, A. Alù, A. Toscano, and F. Bilotti, "Surface impedance modeling of all-dielectric metasurfaces," *IEEE Trans. Antennas Propag.*, vol. 68, no. 3, pp. 1799–1811, Mar. 2019.

[23] R. Garcia-Molina, A. Maradudin, and T. Leskova, "The impedance boundary condition for a curved surface," *Phys. Rep.*, vol. 194, nos. 5–6, pp. 351–359, 1990.

[24] D. Sievenpiper, L. Zhang, R. F. J. Broas, N. G. Alexopolous, and E. Yablonovitch, "High-impedance electromagnetic surfaces with a forbidden frequency band," *IEEE Trans. Microw. Theory Techn.*, vol. 47, no. 11, pp. 2059–2074, Nov. 1999.

[25] J.-R. Poirier, A. Bendali, and P. Borderies, "Impedance boundary conditions for the scattering of time-harmonic waves by rapidly varying surfaces," *IEEE Trans. Antennas Propag.*, vol. 54, no. 3, pp. 995–1005, Mar. 2006.

[26] J. N. Reddy, *Introduction to the Finite Element Method*. New York, NY, USA: McGraw-Hill, 2019.

[27] P. H. Pathak and R. Kouyoumjian, "The radiation from apertures in curved surfaces," NASA, Washington, DC, USA, Tech. Rep. NASA CR-2263, 1973.

[28] M. D. Casciato and K. Sarabandi, "High-frequency radio wave diffraction from singly curved, convex surfaces—A heuristic approach," *IEE Proc.-Microw., Antennas Propag.*, vol. 151, no. 1, pp. 43–53, 2004.

[29] C. L. Holloway and E. F. Kuester, "Power loss associated with conducting and superconducting rough interfaces," *IEEE Trans. Microw. Theory Techn.*, vol. 48, no. 10, pp. 1601–1610, Oct. 2000.

[30] S. Luo, J. Hao, F. Ye, J. Li, Y. Ruan, H. Cui, W. Liu, and L. Chen, "Evolution of the electromagnetic manipulation: From tunable to programmable and intelligent metasurfaces," *Micromachines*, vol. 12, no. 8, p. 988, 2021.

[31] G. E. Bonacchini and F. G. Omenetto, "Reconfigurable microwave metadevices based on organic electrochemical transistors," *Nature Electron.*, vol. 4, no. 6, pp. 424–428, 2021.

[32] P. Gaire, V. Jaiswal, S. Y. B. Sayeed, J. L. Volakis, M. R. Pulugurtha, and S. Bhardwaj, "Tunable multiferroics for reconfigurable RF system packages," in *Proc. IEEE 16th Nanotechnol. Mater. Devices Conf. (NMDC)*, Dec. 2021, pp. 1–4.

[33] M. Qiao, X. Lei, Y. Ma, L. Tian, X. He, K. Su, and Q. Zhang, "Application of yolk–shell Fe_3O_4@ N-doped carbon nanochains as highly effective microwave-absorption material," *Nano Res.*, vol. 11, no. 3, pp. 1500–1519, 2018.

[34] A. M. Patel, "Controlling electromagnetic surface waves with scalar and tensor impedance surfaces," Ph.D. dissertation, Dept. Elect. Eng. Comput. Sci. (EECS), Univ. Michigan, Ann Arbor, MI, USA, 2013.

[35] OpenStreetMaps Contributors. *3D Model of the Buildings Used in Section 5*. [Online]. Available: https://www.openstreetmap.org/

[36] M. Enescu, *5G New Radio: A Beam-Based Air Interface*. Hoboken, NJ, USA: Wiley, 2020.

[37] S. L. Cotton, W. G. Scanlon, and B. K. Madahar, "Millimeter-wave soldier-to-soldier communications for covert battlefield operations," *IEEE Commun. Mag.*, vol. 47, no. 10, pp. 72–81, Oct. 2009.

[38] T. S. Rappaport, *Wireless Communications: Principles and Practice*, vol. 2. Upper Saddle River, NJ, USA: Prentice-Hall, 1996.

[39] L. He, M. G. Amin, C. Reed, and R. C. Malkemes, "A hybrid adaptive blind equalization algorithm for QAM signals in wireless communications," *IEEE Trans. Signal Process.*, vol. 52, no. 7, pp. 2058–2069, Jul. 2004.

[40] S. L. Cotton, "Human body shadowing in cellular device-to-device communications: Channel modeling using the shadowed κ-μ fading model," *IEEE J. Sel. Areas Commun.*, vol. 33, no. 1, pp. 111–119, Jan. 2015.

[41] J. Kibiłda, A. B. MacKenzie, M. J. Abdel-Rahman, S. K. Yoo, L. G. Giordano, S. L. Cotton, N. Marchetti, W. Saad, W. G. Scanlon, A. Garcia-Rodriguez, D. López-Pérez, H. Claussen, and L. A. DaSilva, "Indoor millimeter-wave systems: Design and performance evaluation," *Proc. IEEE*, vol. 108, no. 6, pp. 923–944, Jun. 2020.

SIMON L. COTTON (Senior Member, IEEE) received the B.Eng. degree in electronics and software from Ulster University, Ulster, U.K., in 2004, and the Ph.D. degree in electrical and electronic engineering from Queen's University Belfast, Belfast, U.K., in 2007. From 2007 to 2011, he was a Research Fellow, then a Senior Research Fellow, from 2011 to 2012, a Lecturer (Assistant Professor), from 2012 to 2015, and a Reader (Associate Professor), from 2015 to 2019, at Queen's University Belfast. He is currently a Full Professor and the Director of the Centre for Wireless Innovation (CWI), Queen's University Belfast. He has authored or coauthored over 150 publications in major IEEE/IET journals and refereed international conferences, two book chapters, and two patents. Among his research interests are propagation measurements and statistical channel characterization. His research interests include cellular device-to-device, vehicular, and body-centric communications. He was awarded the H. A. Wheeler Prize, in July 2010, by the IEEE Antennas and Propagation Society for the Best Applications Journal Paper in the IEEE Transactions on Antennas and Propagation in 2009. In July 2011, he was awarded the Sir George Macfarlane Award from the U.K. Royal Academy of Engineering in recognition of his technical and scientific attainment since graduating from his first degree in engineering.

MUHAMMAD ALI BABAR ABBASI (Member, IEEE) received the B.S. degree in electrical engineering from COMSATS University Islamabad (CUI), Pakistan, the M.S. degree in electrical engineering from the National University of Sciences and Technology (NUST), Islamabad, Pakistan, in 2013, and the Ph.D. degree in electrical engineering from Frederick University, Nicosia, Cyprus, in 2017. From 2017 to 2019, he held a Research Fellowship with the Centre of Wireless Innovation (CWI), Queen's University Belfast (QUB), Belfast, U.K. He is currently a Lecturer (Assistant Professor) with QUB. He has authored or coauthored over 70 journals and conference papers and contributed five book chapters. He was a recipient of the Erasmus Mundus INTACT Doctoral Scholarship by the European Union in 2014. He has been an IEEE Antennas and Propagation Society (AP-S) Young-Professional Ambassador since 2022, IET-Young-Professional since 2017, and a Grand Prize Winner of the Mobile World Scholar Challenge at the Mobile World Congress (MWC) 2019. He acted as a publication chair, a session chair, a technical program committee member, and a reviewers in several scientific conferences and workshops.

GABRIEL G. MACHADO (Member, IEEE) received the B.Sc. degree in electrical engineering from the Federal University of Pernambuco, Recife, Brazil, in 2016, and the Ph.D. degree in microwave engineering from Queen's University Belfast, Belfast, U.K., in 2021. He is currently a Research Fellow with the Centre of Wireless Innovation (CWI), Queen's University Belfast. He has authored or coauthored 21 journals and conference papers and contributed to the writing of two technical book chapters. His research interests include frequency selective surfaces, radiation absorbent materials, phased-array antennas, and sustainable electronics development.

OKAN YURDUSEVEN (Senior Member, IEEE) received the Ph.D. degree in electrical engineering from Northumbria University, Newcastle upon Tyne, U.K., in 2014. He is currently a Reader (Associate Professor) at the School of Electronics, Electrical Engineering and Computer Science, Queen's University Belfast, U.K. Prior to this, he was a NASA Research Fellow at the NASA Jet Propulsion Laboratory, California Institute of Technology, USA. He is also an Adjunct Professor at Duke University, USA. His research interests include microwave and millimeter-wave imaging, multiple-input–multiple-output (MIMO) radars, wireless power transfer, antennas and propagation, and metamaterials. He has authored more than 150 peer-reviewed technical journals and conference papers, and has been a principal investigator and a co-investigator on research grants totaling in excess of £10M in these fields. He is a member of the European Association on Antennas and Propagation (EurAAP). He was a recipient of several awards, including an Outstanding Postdoctoral Researcher at Duke University Award in 2017, the Duke University Professional Development Award in 2017, the NASA Postdoctoral Program Award in 2018, British Council–Alliance Hubert Curien Award in 2019, the Leverhulme Trust Research Leadership Award in 2020, the Young Scientist Award from the Electromagnetics Academy–Photonics and Electromagnetics Research Symposium in 2021, and the Queen's University Belfast Vice Chancellor's Early Career Researcher Prize in 2022. He serves as an Associate Editor for the IEEE ANTENNAS AND WIRELESS PROPAGATION LETTERS, *Scientific Reports* (Nature), and *Remote Sensing* (MDPI).

● ● ●